ACS NANO

www.acsnano.org

ARTICLE

Are 2D Interfaces Really Flat?

Zhihui Cheng,* Huairuo Zhang, Son T. Le, Hattan Abuzaid, Guoqing Li, Linyou Cao, Albert V. Davydov, Aaron D. Franklin,* and Curt A. Richter*

Cite This: *ACS Nano* 2022, 16, 5316–5324

Read Online

ACCESS | Metrics & More | Article Recommendations | Supporting Information

ABSTRACT: Two-dimensional (2D) van der Waals materials are subject to mechanical deformation and thus forming bubbles and wrinkles during exfoliation and transfer. A lack of interfacial "flatness" has implications for interface properties, such as those formed by metal contacts or insulating layers. Therefore, an understanding of the detailed properties of 2D interfaces, especially their flatness under different conditions, is of high importance. Here we use cross-sectional scanning transmission electron microscopy (STEM) to investigate various 2D interfaces (2D-2D and 3D-2D) under the effects of stacking, atomic layer deposition (ALD), and metallization. We characterize and compare the flatness of the hBN-2D and metal-2D interfaces down to angstrom resolution. It is observed that the dry transfer of hexagonal boron nitride (hBN) can dramatically alter the interface structure. When characterizing 3D metal-2D interfaces, we find that Ni-MoS_2 interfaces are more uneven and have larger nanocavities compared to other metal-2D interfaces. The electrical characteristics of a MoS_2-based field-effect transistor are correlated to the interfacial transformation in the contact and channel regions. The device transconductance is improved by 40% after the hBN encapsulation, likely due to the interface interactions at both the channel and contacts. Overall, these observations reveal the intricacy of 2D interfaces and their dependence on the fabrication processes.

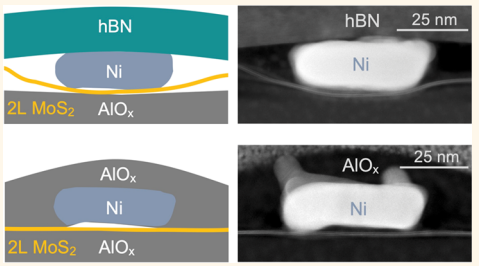

KEYWORDS: *2D interfaces, flatness, strain, nanogaps, nanocavities, MoS_2, hBN*

Two-dimensional (2D) van der Waals materials offer a fertile platform for potential use in future electronics and photonics applications. The fundamental building blocks for research in these areas are the 2D interfaces, including 2D-2D and 2D-3D interfaces.[1,2] Understanding the 2D-2D interfaces is essential for studying emergent phenomena, as exemplified by the surge of recent interest in emergent electron correlation and topology from stacked and twisted 2D heterostructures.[3,4] 2D-3D interfaces are also of paramount importance; for example, the high contact resistance of metal-2D contacts has been the main limiting factor for improving the performance of transistors based on 2D materials.[5] 2D interfaces have been investigated by using a plethora of characterization techniques, including Raman and photoluminescence (PL) spectroscopy, X-ray photoelectron spectroscopy (XPS), transmission electron microscopy (TEM), and force friction microscopy (FFM). Together these studies shed light on the fundamental properties of 2D materials and interfaces in 2D heterostructures, ranging from material interaction,[6] excitonic behaviors,[7,8] defect dynamics,[9,10] and interlayer adhesion and friction.[11]

While the wrinkle,[12] delamination, and buckle[13] of standalone 2D materials have been investigated, studies on the overall morphology and flatness of 2D interfaces have been sparse. Atomic force microscopy (AFM)[12] and piezoresponse force microscopy (PFM)[14] have been utilized to map top surfaces of 2D heterostructures. These approaches can cover large areas of materials and provide topographical information, but they do not directly probe the buried interfaces and thus do not reveal sufficient interface insight. Optoelectronic imaging of the 2D-semiconductor−3D metal buried interfaces has been conducted,[15] but the detailed interface profile remains uninvestigated. The van der Waals interface between 2D materials and 3D metal contacts (indium) has been visualized by TEM, but the images were presented on a scale of a few nanometers to characterize the local atomic bonding.[16] Our study intends to expand the viewpoint on the 2D interfaces in two aspects: (1) the direct imaging of the cross-sectional interfaces at the total length scale of 12.5 μm and (2) how 2D interfaces can be impacted by staking, atomic layer deposition (ALD), and metallization, which are the most common processes used in 2D materials and device research nowadays.

Here we use "Z-contrast" high-angle annular dark-field scanning transmission electron microscopy (HAADF-STEM)

Received: December 24, 2021
Accepted: March 3, 2022
Published: March 15, 2022

https://doi.org/10.1021/acsnano.1c11493
ACS Nano 2022, 16, 5316–5324

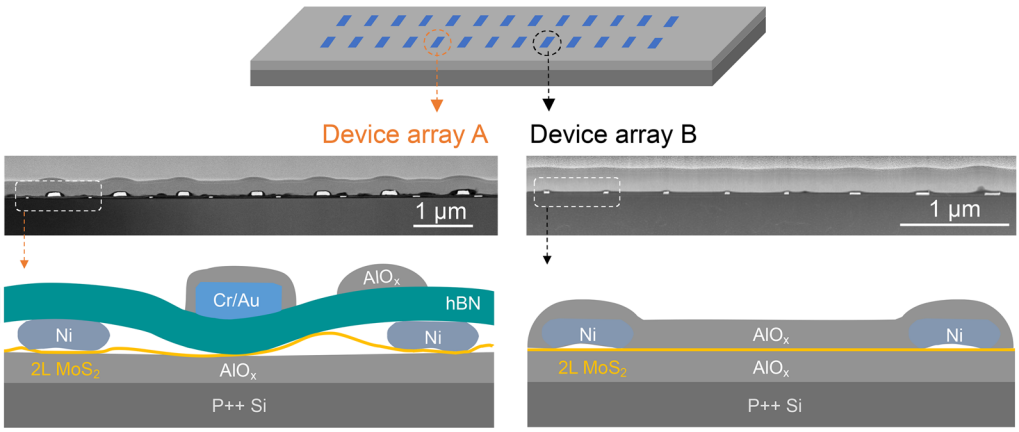

Figure 1. Illustration of Device arrays A and B with corresponding cross-sectional STEM images. An example diagram of a transistor on each array is also given underneath the STEM images. Device arrays A and B have a total length of 8 and 4.5 μm, respectively. The process flow of fabricating the device arrays is given in the Methods and Figure S1. Briefly, the hBN was dry transferred onto fabricated devices in Device array A and then Cr/Au metal gates were fabricated onto the hBN. Afterward, the entire sample went through atomic layer deposition (ALD) to grow the AlO_x on top.

to examine the cross-sectional structure of various 2D interfaces on the length scale of an array of electronic devices (~12.5 μm in total). Contrary to the conventional assumption that 2D interfaces are always flat, we find that these interfaces can be quite intricate and complex. Correlating the interface deformation with the corresponding device performance, we discover how the nonplanar interfaces can affect the device characteristics. Our results have direct implications for devices where 2D materials are transferred onto patterned contacts and for devices where metal contacts are deposited onto 2D materials. These devices include the common top- or bottom-contacted transistors[17] and bottom-contacted Hall bars,[18,19] where edge contacts may have poor performance.

RESULTS AND DISCUSSION

The 2D interfaces studied here come from two device arrays: Device array A and B. The illustration of the two device arrays is shown in Figure 1. We define the interfaces between two different 2D-layered materials as 2D-2D interfaces. In Device array A, the 2D-2D interface is the hBN-MoS_2 in the channel region. Similarly, 3D-2D interfaces represent the interfaces between 3D materials and 2D materials. In a typical 2D transistor, the 3D-2D interfaces include the 3D metal-2D contact interface and 3D dielectric-2D interface. These 3D-2D interfaces can be found in both Device array A and B.

2D-2D Interfaces. Dry transferring and stacking 2D materials is a common approach to fabricate 2D heterostructure interfaces.[20] In these interfaces, hBN is widely used as an encapsulation layer for various systems, from transistors[17,21,22] to twisted 2D bilayers.[3,18] Figure 2a,b shows the transferred hBN on top of fabricated MoS_2 field-effect transistors (FETs) in Device array A. In the array, seven adjacent transistors, each with a channel length of ~940 nm, are fabricated on the same bilayer MoS_2 film. A STEM image of the Device array A is given in Figures 1 and S2, which shows the eight adjacent contact electrodes. The hBN does not transfer conformally in the 3D metal contact region (Figure 2c). Rather, the hBN stacking process presses the contact metal downward, inducing strain at the Ni-MoS_2 contact interface. Underneath the Ni contact, the ALD AlO_x exhibits a reduced thickness of ~17 nm compared to its initial thickness of 20 nm—an effect of the amorphous nature of the AlO_x, making it prone to external pressures. Different oxides with different thicknesses and grown using other methods may respond differently to external pressures. The detailed comparison of these mechanical responses at 2D interfaces merits further studies.

The hBN transfer and stacking process also caused the MoS_2 to arc upward as high as 10 nm on the right side of the contact metal in Figure 2c. This arc deformation introduces additional strain, potentially impacting device performance. The 25 nm thick hBN demonstrates some flexibility with a bending region spanning ~200 nm on one side. The spanning length largely depends on the metal contact thicknesses and the thickness/stiffness of the hBN. A graphene bilayer has been shown to conform to a 4 nm hBN step[23] and thinner 2D materials are less stiff.[24] Hence, a thinner hBN may conform more closely to thin metal contacts, producing a shorter bending region. The detailed adhesion and friction energies of the hBN-metal interface warrant further study. More STEM images of the hBN encapsulated contact areas and the statistical analysis of bending regions can be seen in Figure S3.

Further into the channel region (away from the contacts), the MoS_2-hBN and MoS_2-AlO_x interfaces tend to be relatively flat (Figure 2d), where the flatness is defined on the scale of a nanometer. Specifically, the hBN-MoS_2-AlO_x interface tends to be flat and intimate at the center of the channel, as shown in Figure 2d(i) and Figure S4. In the channel region closer to the contacts, hBN and MoS_2 start to separate, forming nanogaps of different heights. Notably, in Figure 2d(ii), the MoS_2 is in close contact with the underlying AlO_x, whereas in Figure 2d(iii), the hBN "picks up" the MoS_2 for ~2.4 nm upward from the AlO_x on the left side of the image due to van der Waals attraction. This observed hBN-MoS_2 interaction demonstrates that nanogaps can also be formed between MoS_2 and the underlying substrate. Figure 2d also indicates that with sufficiently long channels, the impact of nonflatness is more concentrated at the contacts; however, when channel lengths are scaled, there will be considerable effects on the channel/gate region itself. These observations highlight that the stacking process widely used in 2D heterostructure studies can drastically alter the flatness of 2D-2D and 2D-3D interfaces in the vicinity of metal contacts if the contacts are made before the transfer and stacking steps.

https://doi.org/10.1021/acsnano.1c11493
ACS Nano 2022, 16, 5316−5324

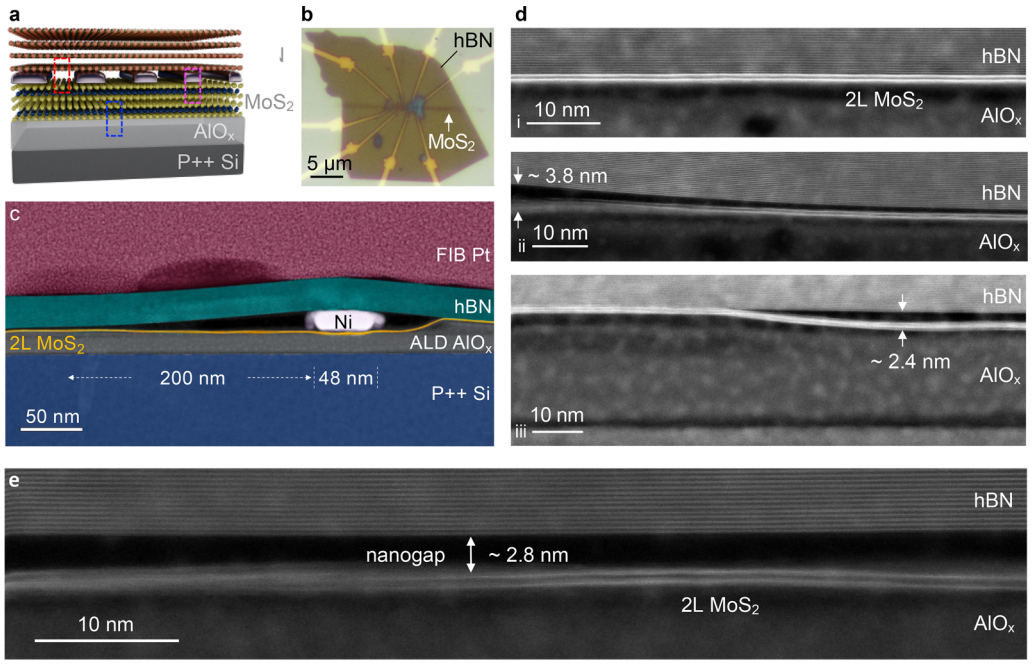

Figure 2. Schematics and HAADF-STEM images of the hBN-MoS_2-AlO_x interface in Device array A. (a) Cross-sectional schematic of the device. The red, blue, and magenta dashed boxes represent hBN-MoS_2, MoS_2-AlO_x, and Ni-MoS_2 interfaces, respectively. (b) Optical image of the devices with hBN encapsulation. (c) False-colored STEM image of a contact region. The thickness of the Ni contact is ∼16 nm. (d) The hBN-MoS_2 and MoS_2-AlO_x interfaces in the channel region with (i–iii) representing different locations. In (i), the interfaces are flat and intimate, whereas in (ii–iii), the hBN and MoS_2 diverge to form nanogaps. (e) An example nanogap of ∼2.8 nm formed between hBN and 2L MoS_2 in the channel region. The detailed location of the area is shown in Figure S2.

Substantial length of nanogaps between hBN-MoS_2 can form in the channel region, as illustrated in Figures 2d,e and S2. Such nanogaps were observed in three out of the seven channels and ranged from 2.8 to 4.2 nm in height and extended to ∼560 nm in length on average, highlighting that the impact of the transfer process can extend well beyond the contact region. Due to the cross-sectional nature of the STEM imaging, the exact area of the nanocavities formed by these nanogaps is unknown. In these nanogaps, the 2L MoS_2 is not as flat, without the intimate vdW interface to the hBN, compared to the areas where the 2L MoS_2 is in direct contact with the hBN. For example, the 2L MoS_2 in Figure 2e is flatter relative to Figure 2d(i), with RMS roughness increasing from 0.1 to 0.2 nm (nanogap 2 in Figure S2 has a similar nanogap height but with an RMS roughness of ∼0.4 nm).

Several mechanisms are examined for the increased roughness. First, the underlying AlO_x is not a contributing factor to the MoS_2 flatness or roughness, as seen from Figures 2e and S2. Second, during STEM imaging, the electron irradiation may damage and distort the 2L MoS_2, as seen on the left side of Figure 2e. However, on the right side of Figure 2e, the 2D layer integrity remains largely intact, further corroborated by Figure S2, where the nanogap 2 is imaged at a lower magnification and thus with less electron irradiation damage. Both of these regions are still uneven, suggesting that the electron irradiation damage during STEM imaging is not the main factor behind the increased roughness of MoS_2. Finally, due to the elastic nature of the hBN, the hBN may have contacted the MoS_2 first but then detached and returned to a more stable position. In this case, the hBN transfer process would be the main reason for the unevenness of the MoS_2 layers in the nanogaps.

For applications such as nanofluidics where nanogaps are required, controllably producing a uniform nanogap will require co-optimization of multiple factors, such as thinner contact metals and shorter channel lengths. Importantly, these nanogaps are formed without an etching step, and thus the top and bottom surfaces are inherently atomically smooth (but not necessarily flat). Hence, the nanogap created this way may have fewer defects than those using an etching step[2,25,26] showing promise for nanofluidics and airgap-based low-*k* dielectric applications.

3D-2D Interfaces. Two types of 3D-2D interfaces are analyzed here: (i) the interface between 3D dielectric material and MoS_2, and (ii) the interface between the 3D metal contact and MoS_2. First, we focus on the interface between an amorphous high-*k* dielectric (AlO_x) and a 2D material (MoS_2). Producing a high-quality gate dielectric and interface on 2D materials remains a major challenge for fabricating high-performance FETs and large-scale integrated circuits due to uneven nucleation and thickness scaling.[5] AlO_x grown by using atomic layer deposition (ALD) is a commonly used encapsulation dielectric[27] and has been shown to exhibit a doping effect for MoS_2 FETs.[28] The flatness of the interface between amorphous 3D high-*k* dielectrics and 2D interfaces has profound implications for studying strain, defects, trapped charges, and their impact on device performance.

In the device structure shown in Figure 3a, two layers of AlO_x are grown using thermal ALD: (1) the bottom layer before device fabrication and (2) the top layer after device fabrication, characterization, and hBN stacking. No Al seed layer is deposited before the ALD process to observe the ALD process's direct effect on the interface flatness. This consideration is significant as future high-performance transistor technology nodes require high-*k* oxide with

https://doi.org/10.1021/acsnano.1c11493
ACS Nano 2022, 16, 5316–5324

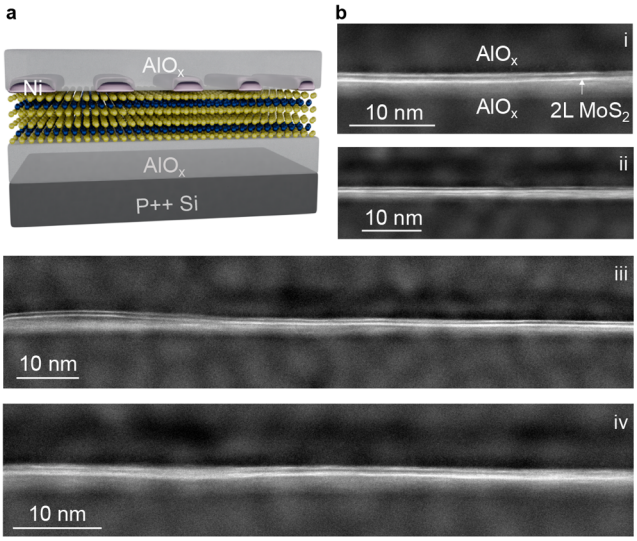

Figure 3. Schematics and HAADF-STEM images of the AlO_x-MoS_2-AlO_x interface in Device array B. (a) Schematic side view of the device structure. The five metal contacts represent the fabricated FET devices before the step of growing top AlO_x layer using ALD. (b) Images of the AlO_x-MoS_2-AlO_x interfaces in the channel region with (i−iv) representing different locations. The interfaces in (i−ii) are slightly flatter than (iii−iv).

equivalent oxide thickness (EOT) less than 1 nm. An Al seed layer would easily oxidize to form a ∼2 nm thick AlO_x film, which already has ∼1 nm of EOT. Hence, observing the impact of ALD films directly deposited on 2D materials is necessary.

Compared to the MoS_2-hBN interface in Figure 2d, the 2D-3D interface (AlO_x-MoS_2) is not as smooth. To quantify the flatness of the interfaces, we developed an approach based on digitizing the cross-sectional STEM images. An illustration of this approach is in Note S1. Briefly, the STEM images are digitized according to the scale bar, allowing us to extract pixel information to sub-angstrom accuracy. Using this approach, the AlO_x-MoS_2 interface is characterized to have an average RMS roughness of 0.1 nm. In comparison, the MoS_2-hBN interface has a slightly smaller average RMS roughness of 0.07 nm, as demonstrated in Figures 2d(i) and S4. Because the hBN-MoS_2-AlO_x interface is intimate in Figures 2d(i) and S4, the small RMS roughness of MoS_2 can be attributed to the flatness of the top hBN and underlying AlO_x. The less flat AlO_x-MoS_2-AlO_x interface can be partially attributed to the top amorphous AlO_x, which is directly nucleated on top of the MoS_2 and thus not as atomically smooth as crystalline hBN. The ALD nucleation process may also introduce interface disorders that affect the 2D crystal at the atomic level. We also note that some parts of the 2L MoS_2 in Figure 3b are slightly obscure compared to Figure 2d, which can be explained by the irradiation effect of the electron beam during the STEM imaging. This effect is more apparent when the imaging magnification is high.

Metal evaporation is commonly used to fabricate metal contacts on 2D materials. Typically, the interface between evaporated metals and the target 2D materials is assumed to be flat. However, as revealed in the STEM images of Figure 4, the 3D-2D interface between the deposited metals and 2D materials is sometimes, surprisingly, not flat. This observation is independent of the contact length (ranging from 38 to 130 nm). Interestingly, in Figure 4a, the Ni on MoS_2 has an arched shape over a relatively flat MoS_2, evidential of low Ni adhesion. The arched Ni contacts produce nanocavities in the middle and van der Waals-like interfaces at the ends of the contact length. The arched Ni contacts also affect the flatness of MoS_2: at the two ends of the Ni contacts, the MoS_2 is "pressed down" and displaced by approximately 0.7 nm. This uneven interface indicates that the widely used metal evaporation process can create uneven pressure on atomically thin 2D materials.

Several possible mechanisms are considered for the uneven Ni-MoS_2 interface in Figure 4a. First, this uneven interface cannot be attributed to grain boundaries since the arched shape is present for all lengths of the interface. Second, the sample preparation for STEM imaging is not likely to cause aggressive Ni deformation because the uneven interfaces are limited mainly to the Ni-MoS_2 interface, whereas Au-hBN and Cr-hBN interfaces are significantly flatter. Also, the arched shape of Ni contacts represents uneven deformation, whereas the focused ion beam used to prepare the sample should have a more even impact across the interface. Third, the adhesion between Ni and MoS_2 likely depends on the surface energies of the materials and their interaction. In Smyth et al.,[6] using XPS, Ti_xS_y was found to form at the Ti-MoS_2 interface, leading to the expected good adhesion. Although NiS exists in nature, whether it can be formed in the Ni-MoS_2 interface remains unclear.

Typically, the smoothness of the metal-oxide interface depends on the reaction between the metal and oxide, which is why Ti and Cr are commonly used adhesion layers for oxides such as SiO_2. However, the wettability of e-beam evaporated metals on 2D materials remains largely unknown (a more detailed discussion is in Note S2). The adhesion is also likely related to surface defects and dislocations at the interface, which promote covalent bonds. The impact of other factors such as the fabrication technique (thermal evaporation vs e-beam evaporation) and the thickness of the metal or 2D materials also merits further study. Lastly, atomistic modeling can help understand the thermodynamics of this interface and its adhesion energies.

Compared to AlO_x encapsulation from Figure 4a, encapsulation of Ni-MoS_2 contacts with transferred hBN results in a more aggressively deformed interface at and surrounding the contact region (Figure 4b). More examples of the hBN encapsulated contact regions can be seen in Figure S3. Qualitatively, Ni merges more with MoS_2 in Figure 4b compared to the more distinct boundary between Ni and MoS_2 in Figure 4a. The pressure applied during the hBN dry transfer process decreases the overall Ni-MoS_2 gap height by 0.6 nm (Figure 4d). This observation suggests that the arc shape of Ni contacts can respond to the applied pressure.

These uneven Ni-MoS_2 interfaces in Figure 4a challenge the conventional assumption that metal-2D interfaces are always flat. To compare the influence of metal type and 2D thickness on the flatness of 3D-2D interfaces, we also examined Cr-hBN and Au-hBN interfaces shown in Figure 4c. In contrast to the Ni-MoS_2 interfaces, these Cr-hBN and Au-hBN interfaces are significantly flatter. The metals, including Ni, Cr, and Au, were deposited in the same electron-beam evaporator. Cr is commonly used as an adhesion layer for glass and oxidized silicon substrates. Importantly, we note that the Cr-hBN nanogaps are likely not made of air but chromium oxides, which appear dark in the HAADF STEM images. Oxides appearing dark in HAADF STEM are also observed for AlO_x

https://doi.org/10.1021/acsnano.1c11493
ACS Nano 2022, 16, 5316−5324

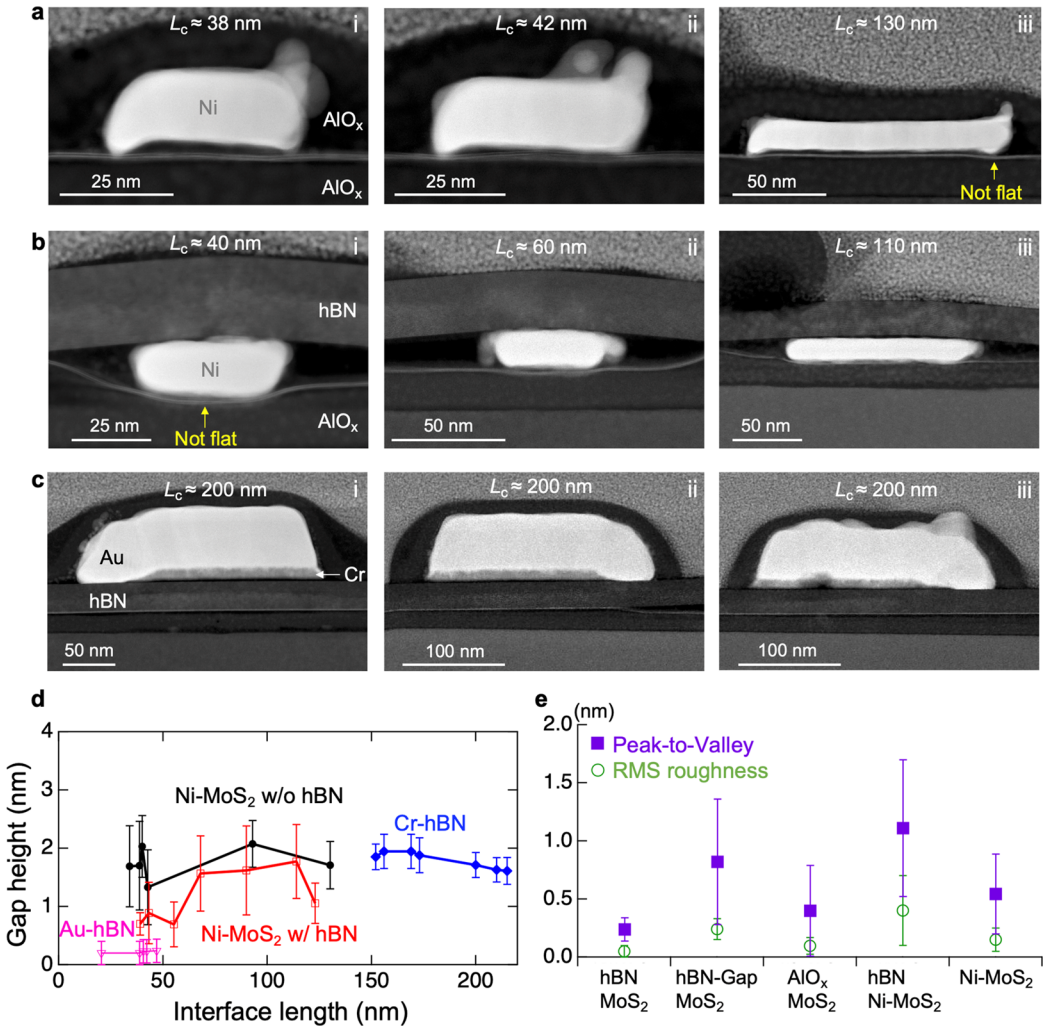

Figure 4. STEM examination of the flatness of 3D metal-2D interfaces. (a) With AlO_x encapsulation on top, Ni contacts on MoS_2 with different L_c. These Ni-MoS_2 interfaces come from Device array B. (b) With hBN encapsulation on top, Ni contacts on MoS_2 different L_c. (c) Cr-hBN and Au-hBN interfaces. The Cr adhesion layer does not cover the entire contact length, which is attributed to a slanted PMMA profile after e-beam lithography and development. Both b and c come from Device array A. (d) Nanogap height of different 3D metal-2D interfaces. The error bars represent one standard deviation of the gap height at the interfaces. The Cr-hBN nanogaps are likely made of chromium oxides, not air. (e) Comparison of the Peak-to-Valley and RMS roughness of the MoS_2 at multiple interfaces. The hBN-MoS_2 interface is in the channel region, away from the contact region. "hBN-Gap-MoS_2" indicates that there are hBN and nanogap on top of the MoS_2. The error bars reflect one standard deviation from the mean value.

and SiO_2 (Figure S5). Compared to Ni and Au, Cr is easily oxidized. The Cr-hBN nanogaps indicate that chromium oxides can be expected at the Cr-2D interface when using Cr as the contact metal for 2D FETs. The Au-hBN is the flattest surface without a gap at the interface (Figures 4c and 4d). The flatness of the 25 nm thick hBN has not changed because of the Cr and Au presence, suggesting that the thicker the 2D material, the less likely its flatness will be affected, similar to the scenario of depositing metal onto bulk materials. Finally, from Figures 4a and 4c, the top surface of the metal contacts does not correlate well to the interface profile and cannot reveal the nanogap information. Hence, we caution against using surface topography measurements alone to represent the buried interfaces.

Although a limited number of metal types and 2D materials are characterized, the interfaces we covered highlight the important role of different material types and thicknesses. Across different interface lengths, the Ni-MoS_2 interface has a much larger standard deviation of nanogap heights than Cr-hBN and Au-hBN interfaces, further underlining the unevenness of the Ni-MoS_2 interface. For Ni-MoS_2 interfaces, the hBN transfer process to encapsulate the structures largely increases the root-mean-square (RMS) roughness of the interface, from ~0.15 nm to ~0.4 nm (Figure 4e). Meanwhile, the MoS_2 has a slightly larger RMS roughness in hBN-Gap-MoS_2 than other 2D-2D and 3D-2D interfaces except for the hBN-Ni-MoS_2 interface.

Unlike RMS roughness, which represents the overall flatness, Peak-to-Valley values highlight the extreme cases in different images. The average RMS roughness and Peak-to-Valley values are correlated, with hBN-Ni-MoS_2 being the roughest and hBN-MoS_2 the flattest. Not surprisingly, the hBN-Ni-MoS_2 has the biggest standard deviation because of the aggressive mechanical pressure from the hBN stacking process. Without hBN encapsulation, the nonflatness of AlO_x-MoS_2 and Ni-MoS_2 interfaces may have an unexpected impact on the interface property and thus device performance. Hence, further

https://doi.org/10.1021/acsnano.1c11493
ACS Nano 2022, 16, 5316−5324

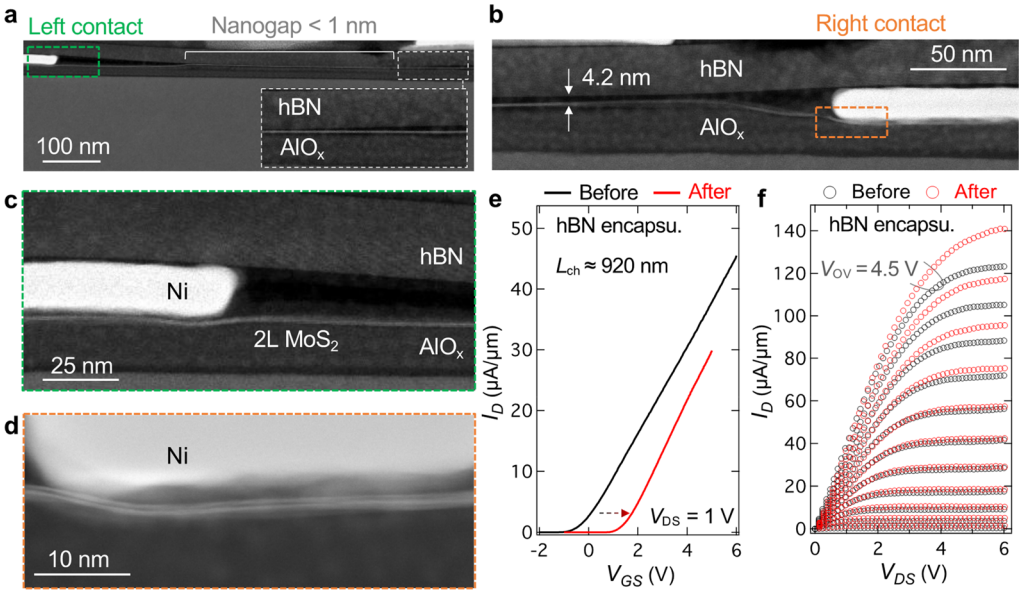

Figure 5. Comparison of transistor performance before and after hBN encapsulation. Cross-sectional HAADF-STEM image of (a) left and (b) right contact of the example device. Magnified image of the left (c) and right (d) contact interfaces post-hBN encapsulation. (e) I_D−V_{GS}, and (f) I_D−V_{DS} of the exact same back-gated device before and after hBN encapsulation. The back-gate oxide is 20 nm AlO_x. Overdrive voltage, $V_{OV} = V_{GS} - V_{TH}$, is from 4.5 V to −0.5 V in steps of 0.5 V.

investigation of different fabrication procedures is needed to study, understand, and improve 2D interface flatness.

Device Implications. For the same FET device made of C7 (left contact) and C8 (right contact) in Figure S2, the device characteristics before and after hBN encapsulation are compared. The left and right contacts of the device are respectively given in Figure 5a,b. In Figure 5a, around 375 nm of the channel has a negligible nanogap (<1 nm), and then the nanogap gradually expands to 4.2 nm near the right contact, as seen in Figure 5a,b. This observation shows the encapsulation of the channel is not complete, similar to the nanogaps in Figure S2. The incomplete encapsulation effect is usually ignored in other stacking and encapsulation studies.[17,29] Using Raman and PL spectroscopy, hBN encapsulation of MoS_2 has been shown to change the property of MoS_2.[30] The addition of the nanogap between the hBN and MoS_2 likely further modifies the optical and electrical properties of the MoS_2. In Figure 5c,d, the deformation of MoS_2 near the metal contact is also apparent, congruent with the observations in Figure 4.

Figure 5e shows a positive V_{TH} shift of ∼1.6 V and increased transconductance (g_m) by ∼40% post-hBN encapsulation (from ∼8.5 μS/μm to ∼12 μS/μm). Since field-effect mobility (μ_{FE}) can be estimated using $\frac{Lg_m}{WC_{ox}V_{DS}}$, μ_{FE} also increased by 40% from 15.2 to 21.4 $cm^2\ V^{-1}\ s^{-1}$. To adjust for the V_{TH} shift, Figure 5f plots the output curves at different overdrive voltages. Because of the improved transconductance, the drain current increased 14%, from 122 μA/μm to 140 μA/μm at V_{DS} = 6 V and V_{OV} = 4.5 V (carrier density ≈7.9×10^{12} cm^{-2}). We attribute these changes to multiple factors, including reduced adsorbent-type trapping sites post-hBN encapsulation and the induced strain near/at the contact interface.

Also, in Figure 5b,c, the bilayer MoS_2 channel near the contacts bends away from the substrate. The partially floating channel introduces an airgap between the MoS_2 and the substrate, thus adding a capacitance in series with the AlO_x capacitance. This structure reduces the total capacitance, decreasing the gate electrostatic control, which contradicts the improved transconductance in Figure 5e. Hence, the floating channel near the contacts may not be the major factor behind the device performance improvement. The specific relationship between fabrication techniques, physical interfaces, and device performance merits further examination. Meanwhile, among the seven devices in the array, only one device presented in Figure 5 functions normally after the hBN stacking and ALD process steps. This low yield could be related to the annealing effect of the ALD process at 120 °C.[27] Hence, statistical representation of the performance increase also warrants future studies.

CONCLUSIONS

In summary, we have revealed the intricacy of various 2D interfaces at the length scale of a device array (12.5 μm in total) and under the impact of stacking and metallization. The hBN stacking process clearly has a mechanically aggressive effect on the flatness of the interfaces and films. The metal deposited from the commonly used e-beam evaporator can also distort the Ni-MoS_2 interface, especially near the contact edge where there is more pressure due to the arc shape of the contacts. These observations have broad implications in applications such as electronic devices and nanofluidics. Moving forward, the delicate nature of 2D interfaces should be considered when characterizing their properties. Strain and interface engineering show promise for contact engineering and device performance optimization. These effects will be especially pronounced for devices that involve transferring and stacking 2D materials onto predeposited metal contacts or gates. Finally, the nonflat Ni-MoS_2 interface provides insights for contact engineering where metallization onto 2D materials using physical vapor deposition is prevalent. The results of this study will help develop a deeper understanding of 2D interfaces and interface engineering.

https://doi.org/10.1021/acsnano.1c11493
ACS Nano 2022, 16, 5316−5324

METHODS

Device Fabrication and Electrical Characterization. An illustration of the device fabrication process flow is given in Figure S1. As covered in ref 31, MoS_2 was grown using chemical vapor deposition at 750 °C for 10 min under a flow of argon gas at a rate of 100 sccm at ambient pressure. The MoS_2 film was then transferred onto AlO_x (grown by ALD at 120 °C[27]) on a p++ Si substrate to reduce the substrate coupling compared to MoS_2 on as-grown substrate.[32] Sixteen nm of Ni contacts were then fabricated onto the MoS_2 using e-beam lithography and e-beam evaporation. The e-beam evaporator (CHA Solution) has a source distance of 15 in. The evaporation pressure is $\sim 2 \times 10^{-6}$ Torr and the evaporation rate is ~1 Å per second. The devices were measured twice—before and after the hBN stacking process. Then, intended as top gate, 10 nm Cr/50 nm Au gate electrodes were fabricated on top of the hBN (the evaporation rate, ~2 Å per second). Finally, a top layer of AlO_x was grown onto the sample using ALD before preparing for STEM imaging. No Al seed layer has been deposited before the ALD.

During electrical characterization, the sample was placed inside the Lakeshore CRX-6.5 K probe station and was measured using Keysight B1500 as the analyzer at room temperature and low vacuum ($\sim 1 \times 10^{-3}$ Torr).

hBN Stacking. For Device array A, after electrically characterizing the devices first, hexagonal boron nitride (hBN) was transferred onto the device array. Using a process similar to refs 33, 34, the hBN is picked up and transferred using a polypropylene carbonate (PPC) and polydimethylsiloxane (PDMS) stacking station. In short, a PDMS cube of about ~1 mm thick and about 2 mm by 2 mm in width and length is placed on a 3 by 1 in. microscope slide. A transparent scotch tape is then placed on top of the PDMS and the glass. The tape is gently pressed down around the PDMS, making the PDMS into a convex shape. PPC is then placed on top of the formed PDMS to complete the stacking stamp. The convex-shaped stamp allows for precise position and placement control of the stamp during the stacking steps. Using the PDMS/PPC stamp, mounted on a micropositioning stage, exfoliated hBN is picked up from oxidized silicon substrate at about ~40 °C. After aligning the hBN with Device array A and bringing the hBN and stamp into close contact with the Device, the whole setup is heated to ~100 °C at a rate of about 4 to 5 °C per minute. The stamp thermally expands and slowly brings the hBN onto physical contact with the devices at a controllable rate. This approach allows for almost bubble-free transfer and ultimate contact between the devices and the hBN. The transferring process takes approximately 30 min. At 100 °C, a portion of the PPC that contacts the substrate is melted and stays on the substrate with the hBN while the stamp is slowly retracted from the substrate to complete the transfer. After the transfer, the leftover PPC is annealed in a vacuum chamber (base pressure, $\sim 3 \times 10^{-6}$ Torr) at the temperature of 350 °C for 1 h.

HAADF-STEM Preparation and Characterization. An FEI Nova NanoLab 600 DualBeam (SEM/FIB) was employed to prepare cross-sectional STEM samples. An electron beam-induced Pt deposition around 100 nm was deposited over the device to protect the sample surface, followed by a 2 μm Pt deposition with ion beam. The STEM samples were thinned with 30 kV Ga-ions beam while final thinning was performed at 2 kV to reduce damage. The Z-contrast HAADF-STEM images were collected using an FEI Titan 80−300 probe-corrected STEM/TEM microscope operating at 300 keV, with a beam convergence angle of 20 mrad and collection angles >50 mrad.

ASSOCIATED CONTENT

Supporting Information

The Supporting Information is available free of charge at https://pubs.acs.org/doi/10.1021/acsnano.1c11493.

The process flow of fabricating the device arrays, cross-sectional HAADF-STEM images of Device array A, the hBN encapsulated contact regions in Device array A, flat and intimate hBN-MoS_2-AlO_x interfaces, oxides appearing dark in STEM images, quantifying nanogap height and flatness of MoS_2, the interface between e-beam evaporated metal and 2D materials (PDF)

AUTHOR INFORMATION

Corresponding Authors

Zhihui Cheng − *Nanoscale Device Characterization Division, National Institute of Standards and Technology, Gaithersburg, Maryland 20899, United States; Department of Electrical & Computer Engineering, Purdue University, West Lafayette, Indiana 47907, United States;* orcid.org/0000-0003-1285-0523; Email: cheng511@purdue.edu

Aaron D. Franklin − *Department of Electrical & Computer Engineering, Duke University, Durham, North Carolina 27708, United States; Department of Chemistry, Duke University, Durham, North Carolina 27708, United States;* orcid.org/0000-0002-1128-9327; Email: aaron.franklin@duke.edu

Curt A. Richter − *Nanoscale Device Characterization Division, National Institute of Standards and Technology, Gaithersburg, Maryland 20899, United States;* Email: curt.richter@nist.gov

Authors

Huairuo Zhang − *Materials Science and Engineering Division, National Institute of Standards and Technology, Gaithersburg, Maryland 20899, United States; Theiss Research, La Jolla, California 92037, United States;* orcid.org/0000-0002-1984-1200

Son T. Le − *Nanoscale Device Characterization Division, National Institute of Standards and Technology, Gaithersburg, Maryland 20899, United States; Theiss Research, La Jolla, California 92037, United States*

Hattan Abuzaid − *Department of Electrical & Computer Engineering, Duke University, Durham, North Carolina 27708, United States;* orcid.org/0000-0002-6712-4644

Guoqing Li − *Department of Materials Science and Engineering, North Carolina State University, Raleigh, North Carolina 27695, United States*

Linyou Cao − *Department of Materials Science and Engineering, North Carolina State University, Raleigh, North Carolina 27695, United States;* orcid.org/0000-0002-6235-001X

Albert V. Davydov − *Materials Science and Engineering Division, National Institute of Standards and Technology, Gaithersburg, Maryland 20899, United States*

Complete contact information is available at: https://pubs.acs.org/10.1021/acsnano.1c11493

Author Contributions

Z.C. conceived and designed the experiments. Z.C. fabricated and characterized the devices with the assistance of H.A.; G.L. and L.C. grew the MoS_2. S.L. and Z.C. transferred and stacked the hBN. H.Z. performed the STEM characterization. Z.C., A.D.F., and C.A.R. analyzed the data and wrote the manuscript with input from all authors.

Funding

Z.C. acknowledges financial support from Semiconductor Research Corporation (SRC) nCORE program sponsored by NIST through award number 70NANB17H041. H.A. and A.D.F acknowledge support from the National Science

Foundation (ECCS 1915814). H.Z. acknowledges support from the U.S. Department of Commerce, NIST under financial assistance award 70NANB19H138. A.V.D. acknowledges support from the Material Genome Initiative funding allocated to NIST.

Notes

The authors declare no competing financial interest.

Certain commercial equipment, instruments, or materials are identified in this paper in order to specify the experimental procedure adequately. Such identifications are not intended to imply recommendation or endorsement by the National Institute of Standards and Technology (NIST), nor it is intended to imply that the materials or equipment identified are necessarily the best available for the purpose.

ACKNOWLEDGMENTS

Since fabrication and measurements were partially performed at the NIST Center for Nanoscale Science and Technology and Duke Shared Manufacturing and Instrument Facility (SMIF), we thank the staff at these research facilities for their support.

REFERENCES

(1) Geim, A. K.; Grigorieva, I. V. Van Der Waals Heterostructures. *Nature* **2013**, *499* (7459), 419−425.

(2) Geim, A. K. Exploring Two-Dimensional Empty Space. *Nano Lett.* **2021**, *21* (15), 6356−6358.

(3) Cao, Y.; Fatemi, V.; Demir, A.; Fang, S.; Tomarken, S. L.; Luo, J. Y.; Sanchez-Yamagishi, J. D.; Watanabe, K.; Taniguchi, T.; Kaxiras, E.; Ashoori, R. C.; Jarillo-Herrero, P. Correlated Insulator Behaviour at Half-Filling in Magic-Angle Graphene Superlattices. *Nature* **2018**, *556* (7699), 80−84.

(4) Cao, Y.; Fatemi, V.; Fang, S.; Watanabe, K.; Taniguchi, T.; Kaxiras, E.; Jarillo-Herrero, P. Unconventional Superconductivity in Magic-Angle Graphene Superlattices. *Nature* **2018**, *556* (7699), 43−50.

(5) Cheng, Z.; Price, K.; Franklin, A. D. Contacting and Gating 2-D Nanomaterials. *IEEE Trans. Electron Devices* **2018**, *65* (10), 4073−4083.

(6) Smyth, C. M.; Addou, R.; McDonnell, S.; Hinkle, C. L.; Wallace, R. M. Contact Metal−MoS_2 Interfacial Reactions and Potential Implications on MoS_2-Based Device Performance. *J. Phys. Chem. C* **2016**, *120* (27), 14719−14729.

(7) Gong, Y.; Lin, J.; Wang, X.; Shi, G.; Lei, S.; Lin, Z.; Zou, X.; Ye, G.; Vajtai, R.; Yakobson, B. I.; Terrones, H.; Terrones, M.; Tay, B. K.; Lou, J.; Pantelides, S. T.; Liu, Z.; Zhou, W.; Ajayan, P. M. Vertical and In-Plane Heterostructures from WS_2/MoS_2 Monolayers. *Nat. Mater.* **2014**, *13* (12), 1135−1142.

(8) Bai, Y.; Zhou, L.; Wang, J.; Wu, W.; McGilly, L. J.; Halbertal, D.; Lo, C. F. B.; Liu, F.; Ardelean, J.; Rivera, P.; Finney, N. R.; Yang, X. C.; Basov, D. N.; Yao, W.; Xu, X.; Hone, J.; Pasupathy, A. N.; Zhu, X. Y. Excitons in Strain-Induced One-Dimensional Moiré Potentials at Transition Metal Dichalcogenide Heterojunctions. *Nat. Mater.* **2020**, *19* (10), 1068−1073.

(9) Lin, Z.; Carvalho, B. R.; Kahn, E.; Lv, R.; Rao, R.; Terrones, H.; Pimenta, M. A.; Terrones, M. Defect Engineering of Two-Dimensional Transition Metal Dichalcogenides. *2D Mater.* **2016**, *3* (2), 1−21.

(10) Cheng, Z.; Abuzaid, H.; Yu, Y.; Zhang, F.; Li, Y.; Noyce, S. G.; Williams, N. X.; Lin, Y.-C.; Doherty, J. L.; Tao, C.; Cao, L.; Franklin, A. D. Convergent Ion Beam Alteration of 2D Materials and Metal-2D Interfaces. *2D Mater.* **2019**, *6* (3), 034005.

(11) Dai, Z.; Lu, N.; Liechti, K. M.; Huang, R. Mechanics at the Interfaces of 2D Materials: Challenges and Opportunities. *Curr. Opin. Solid State Mater. Sci.* **2020**, *24* (4), 100837.

(12) Ares, P.; Wang, Y. B.; Woods, C. R.; Dougherty, J.; Fumagalli, L.; Guinea, F.; Davidovitch, B.; Novoselov, K. S. Van Der Waals Interaction Affects Wrinkle Formation in Two-Dimensional Materials. *Proc. Natl. Acad. Sci. U. S. A.* **2021**, *118* (14), e2025870118.

(13) Dai, Z.; Sanchez, D. A.; Brennan, C. J.; Lu, N. Radial Buckle Delamination around 2D Material Tents. *J. Mech. Phys. Solids* **2020**, *137*, 103843.

(14) McGilly, L. J.; Kerelsky, A.; Finney, N. R.; Shapovalov, K.; Shih, E. M.; Ghiotto, A.; Zeng, Y.; Moore, S. L.; Wu, W.; Bai, Y.; Watanabe, K.; Taniguchi, T.; Stengel, M.; Zhou, L.; Hone, J.; Zhu, X.; Basov, D. N.; Dean, C.; Dreyer, C. E.; Pasupathy, A. N. Visualization of Moiré Superlattices. *Nat. Nanotechnol.* **2020**, *15* (7), 580−584.

(15) Jo, K.; Kumar, P.; Orr, J.; Anantharaman, S. B.; Miao, J.; Motala, M. J.; Bandyopadhyay, A.; Kisslinger, K.; Muratore, C.; Shenoy, V. B.; Stach, E. A.; Glavin, N. R.; Jariwala, D. Direct Optoelectronic Imaging of 2D Semiconductor-3D Metal Buried Interfaces. *ACS Nano* **2021**, *15* (3), 5618−5630.

(16) Wang, Y.; Kim, J. C.; Wu, R. J.; Martinez, J.; Song, X.; Yang, J.; Zhao, F.; Mkhoyan, A.; Jeong, H. Y.; Chhowalla, M. Van Der Waals Contacts between Three-Dimensional Metals and Two-Dimensional Semiconductors. *Nature* **2019**, *568* (7750), 70−74.

(17) Islam, A.; Lee, J.; Feng, P. X. L. All-Dry Transferred Single- and Few-Layer MoS_2 Field Effect Transistor with Enhanced Performance by Thermal Annealing. *J. Appl. Phys.* **2018**, *123* (2), 025701.

(18) Wang, L.; Shih, E.-M.; Ghiotto, A.; Xian, L.; Rhodes, D. A.; Tan, C.; Claassen, M.; Kennes, D. M.; Bai, Y.; Kim, B.; Watanabe, K.; Taniguchi, T.; Zhu, X.; Hone, J.; Rubio, A.; Pasupathy, A. N.; Dean, C. R. Correlated Electronic Phases in Twisted Bilayer Transition Metal Dichalcogenides. *Nat. Mater. 2020 198* **2020**, *19* (8), 861−866.

(19) Wang, P.; Yu, G.; Jia, Y.; Onyszczak, M.; Cevallos, F. A.; Lei, S.; Klemenz, S.; Watanabe, K.; Taniguchi, T.; Cava, R. J.; Schoop, L. M.; Wu, S. Landau Quantization and Highly Mobile Fermions in an Insulator. *Nat. 2021 5897841* **2021**, *589* (7841), 225−229.

(20) Yang, R.; Zheng, X.; Wang, Z.; Miller, C. J.; Feng, P. X.-L. Multilayer MoS_2 Transistors Enabled by a Facile Dry-Transfer Technique and Thermal Annealing. *J. Vac. Sci. Technol. B, Nanotechnol. Microelectron. Mater. Process. Meas. Phenom.* **2014**, *32* (6), 061203.

(21) Das, S.; Gulotty, R.; Sumant, A. V.; Roelofs, A. All Two-Dimensional, Flexible, Transparent, and Thinnest Thin Film Transistor. *Nano Lett.* **2014**, *14* (5), 2861−2866.

(22) Lee, G. H.; Cui, X.; Kim, Y. D.; Arefe, G.; Zhang, X.; Lee, C. H.; Ye, F.; Watanabe, K.; Taniguchi, T.; Kim, P.; Hone, J. Highly Stable, Dual-Gated MoS_2 Transistors Encapsulated by Hexagonal Boron Nitride with Gate-Controllable Contact, Resistance, and Threshold Voltage. *ACS Nano* **2015**, *9* (7), 7019−7026.

(23) Han, E.; Yu, J.; Annevelink, E.; Son, J.; Kang, D. A.; Watanabe, K.; Taniguchi, T.; Ertekin, E.; Huang, P. Y.; van der Zande, A. M. Ultrasoft Slip-Mediated Bending in Few-Layer Graphene. *Nat. Mater.* **2020**, *19* (3), 305−309.

(24) Wang, G.; Dai, Z.; Xiao, J.; Feng, S. Z.; Weng, C.; Liu, L.; Xu, Z.; Huang, R.; Zhang, Z. Bending of Multilayer van Der Waals Materials. *Phys. Rev. Lett.* **2019**, *123* (11), 116101.

(25) Radha, B.; Esfandiar, A.; Wang, F. C.; Rooney, A. P.; Gopinadhan, K.; Keerthi, A.; Mishchenko, A.; Janardanan, A.; Blake, P.; Fumagalli, L.; Lozada-Hidalgo, M.; Garaj, S.; Haigh, S. J.; Grigorieva, I. V.; Wu, H. A.; Geim, A. K. Molecular Transport through Capillaries Made with Atomic-Scale Precision. *Nat. 2016 5387624* **2016**, *538* (7624), 222−225.

(26) Keerthi, A.; Goutham, S.; You, Y.; Iamprasertkun, P.; Dryfe, R. A. W.; Geim, A. K.; Radha, B. Water Friction in Nanofluidic Channels Made from Two-Dimensional Crystals. *Nat. Commun. 2021 121* **2021**, *12* (1), 1−8.

(27) Doherty, J. L.; Noyce, S. G.; Cheng, Z.; Abuzaid, H.; Franklin, A. D. Capping Layers to Improve the Electrical Stress Stability of MoS_2 Transistors. *ACS Appl. Mater. Interfaces* **2020**, *12* (31), 35698−35706.

https://doi.org/10.1021/acsnano.1c11493
ACS Nano 2022, 16, 5316−5324

(28) McClellan, C. J.; Yalon, E.; Smithe, K. K. H.; Suryavanshi, S. V.; Pop, E. High Current Density in Monolayer MoS_2 Doped by AlO_x. *ACS Nano* **2021**, *15* (1), 1587−1596.
(29) Illarionov, Y. Y.; Rzepa, G.; Waltl, M.; Knobloch, T.; Grill, A.; Furchi, M. M.; Mueller, T.; Grasser, T. The Role of Charge Trapping in MoS_2/SiO_2 and MoS_2/HBN Field-Effect Transistors. *2D Mater.* **2016**, *3* (3), 035004.
(30) Han, X.; Lin, J.; Liu, J.; Wang, N.; Pan, D. Effects of Hexagonal Boron Nitride Encapsulation on the Electronic Structure of Few-Layer MoS_2. *J. Phys. Chem. C* **2019**, *123* (23), 14797−14802.
(31) Cheng, Z.; Yu, Y.; Singh, S.; Price, K.; Noyce, S. G.; Lin, Y. C.; Cao, L.; Franklin, A. D. Immunity to Contact Scaling in MoS_2 Transistors Using in Situ Edge Contacts. *Nano Lett.* **2019**, *19* (8), 5077−5085.
(32) Alharbi, A.; Huang, Z.; Taniguchi, T.; Watanabe, K.; Shahrjerdi, D. Effect of Substrate Coupling on the Performance and Variability of Monolayer MoS_2 Transistors. *IEEE Electron Device Lett.* **2019**, *40* (1), 135−138.
(33) Kim, K.; Yankowitz, M.; Fallahazad, B.; Kang, S.; Movva, H. C. P.; Huang, S.; Larentis, S.; Corbet, C. M.; Taniguchi, T.; Watanabe, K.; Banerjee, S. K.; Leroy, B. J.; Tutuc, E. Van Der Waals Heterostructures with High Accuracy Rotational Alignment. *Nano Lett.* **2016**, *16* (3), 1989−1995.
(34) Pizzocchero, F.; Gammelgaard, L.; Jessen, B. S.; Caridad, J. M.; Wang, L.; Hone, J.; Bøggild, P.; Booth, T. J. The Hot Pick-up Technique for Batch Assembly of van Der Waals Heterostructures. *Nat. Commun. 2016 71* **2016**, *7* (1), 1−10.

https://doi.org/10.1021/acsnano.1c11493
ACS Nano 2022, 16, 5316−5324